

Article

Tailoring g-C₃N₄ with Lanthanum and Cobalt Oxides for Enhanced Photoelectrochemical and Photocatalytic Activity

Naseer Iqbal 

Department of Chemistry, College of Science, University of Hafr Al Batin, P.O. Box 1803, Hafr Al Batin 39524, Saudi Arabia; naseeriqbal@uhb.edu.sa; Tel.: +966-137208189

Abstract: Herein, the synthesis, characterization, and photoelectrochemical and photocatalytic characteristics of hydrothermally prepared La₂O₃-g-C₃N₄, CoO-g-C₃N₄, and La₂O₃-CoO-g-C₃N₄ are discussed. The XRD analysis and crystalline phases unveiled the impregnation of La₂O₃ and CoO into g-C₃N₄. The microscopic analysis supports the formation of g-C₃N₄ nanoflakes and La₂O₃ and CoO nanoparticles embedded homogeneously in the La₂O₃-CoO-g-C₃N₄ nanocomposite, whereas the EDX comprehended their respective elemental composition and ratios. A bandgap energy of 2.38 eV for La₂O₃-CoO-g-C₃N₄ was calculated using the Tauc plot method, complementing high visible-light activity. The solar-driven water-splitting reaction exhibited significant photocurrent efficiency (~3.75 mA/cm²), augmenting the hydrogen generation by La₂O₃-CoO-g-C₃N₄ compared to that by pure g-C₃N₄, La₂O₃-g-C₃N₄, and CoO-g-C₃N₄ in 0.5 M Na₂SO₄ electrolyte. The synergistic effect of La₂O₃ and CoO impregnation with g-C₃N₄ led to effective division of the photogenerated charge transporters, enhancing the photocatalytic hydrogen generation by the photocatalysts. Furthermore, photocatalytic pollutant removal, namely greater than 90% decomposition of methylene blue (MB) from water, was investigated with a pseudo-first-order reaction kinetics under 1 sun visible-light irradiation. Thus, La₂O₃-CoO-g-C₃N₄ nanocomposite was found to be a prospective material for harnessing solar energy.



Citation: Iqbal, N. Tailoring g-C₃N₄ with Lanthanum and Cobalt Oxides for Enhanced Photoelectrochemical and Photocatalytic Activity. *Catalysts* **2022**, *12*, 15. <https://doi.org/10.3390/catal12010015>

Academic Editors: Zsolt Pap, Lucian Baia and Monica Baia

Received: 13 November 2021

Accepted: 20 December 2021

Published: 24 December 2021

Publisher's Note: MDPI stays neutral with regard to jurisdictional claims in published maps and institutional affiliations.



Copyright: © 2021 by the author. Licensee MDPI, Basel, Switzerland. This article is an open access article distributed under the terms and conditions of the Creative Commons Attribution (CC BY) license (<https://creativecommons.org/licenses/by/4.0/>).

Keywords: carbon nitride; lanthanum cobalt oxide; water splitting; photocatalyst; dye degradation

1. Introduction

In recent years, the fossil-fuel-based economies have been revolving around a major quest for renewable energy sources. Solar-driven water-splitting and environmental remediation are well-reputed, sustainable, clean, and green methods [1–3] generating alternative energy resources. Solar water-splitting for hydrogen and oxygen production is considered a definitive solution for energy and environmental matters. Solar-driven water-splitting or artificial photosynthesis is a concept inspired by natural photosynthesis. It is based on the fabrication of molecular or nanostructured photocatalyst materials to advance our understanding of solar-energy-driven charge distribution and successive photocatalytic water reduction and oxidation processes. Thus, solar fuels can be generated through water, which could potentially address renewable energy and environmental issues. However, from a thermodynamic angle, solar-driven water-splitting is an unfavorable reaction. A positive Gibbs free energy change of 237 kJ mol⁻¹ or 2.46 eV per molecule is required for water-splitting to generate H₂ [4]. To be an effective photocatalyst, the material should possess a sufficiently higher conduction band (CB) and a low valence band (VB) to facilitate the photocatalytic reaction under 1 sun solar irradiation. Numerous photocatalysts are reported in the literature [5,6]; most of them are wideband energy materials having weak photoelectrochemical properties under visible light [7,8]. Alternatively, a variety of photocatalysts are metal-based [9–11], which, on the contrary, are not an eco-friendly and cost-effective solution for alternative energy sources that can be commercialized.

Competent, robust, and low-cost photocatalysts for renewable energy purposes are highly desired for the future of sustainable energy. In this scenario, ample nanomateri-

als have been explored, but research o fabricate excellent photocatalysts is still ongoing. Among those materials, carbon nitrides ($g\text{-C}_3\text{N}_4$) [12], due to their exceptional electrical, semiconducting, photoelectrochemical, and physicochemical properties, are an extensively researched material [13,14]. Besides its fabrication from low-cost precursors, $g\text{-C}_3\text{N}_4$ is a potentially effective and easily implementable photocatalyst. In recent years, phenomenal research has been carried out on metal-free, polymeric, graphitic, carbon nitride ($g\text{-C}_3\text{N}_4$) [15]. It is a non-toxic, affordable semiconductor that can easily be fabricated from precursors of the most abundant elements such as carbon and nitrogen. Graphitic carbon nitride is a metal-free, lightweight, and significantly stable material at ambient conditions [16]. $g\text{-C}_3\text{N}_4$ has good electrochemical properties, chemical and thermal stability, and unique band structure [17,18]. Graphitic- C_3N_4 with and without metal reinforcement is a widely used photocatalyst [5,17–20]. In addition to pure $g\text{-C}_3\text{N}_4$, hybrid- $g\text{-C}_3\text{N}_4$ nanomaterials are also famous for the photocatalytic degradation of organic pollutants in water and air [21–24] as well as for hydrogen production by utilizing solar energy [18,25,26], photocatalytic CO_2 reduction or conversion [17,27,28], and use in ammonia synthesis [29]. However, the photocatalytic activity of pure $g\text{-C}_3\text{N}_4$ still suffers from sluggish conversion efficiencies, rapid electron–hole reassimilation and concurrent charge recombination, diminutive electrical conduction, low optical absorption, and small surface area [30]. Hence, these issues have been addressed lately [31], e.g., fabrication of mesoporous materials [32] and doping of suitable metals or nonmetals [33–36], where induction of metals and hybrid $g\text{-C}_3\text{N}_4$ nanomaterials are introduced.

In recent years, several methodologies have been used to overcome the deficiencies of $g\text{-C}_3\text{N}_4$ materials. Among these, the doping combination of transition metals and rare earth elements enhances their photocatalytic properties. Transition metal oxides of 3d series such as cobalt have been actively used in photocatalytic applications [37,38]. Their wide-scale implementation in photocatalysts can show flexible oxidation states, high catalytic efficacy, and great compatibility. In contrast, the electronic structure of rare earth elements like lanthanum has distinctive spectral characteristics [39,40]. Lanthanum is among the rare earth metals widely applied for doping in nanocomposites for photoelectrochemical applications [41]. Lanthanum ion with its 4*f* electronic configuration can interact with the functional groups with its *f*-orbital [42]. Therefore, it is effective for the improvement of photocatalytic performance. Furthermore, it can be achieved by trapping photogenerated electron–hole pairs to increase their catalytic competence by boosting the separation of photogenerated charge carriers [43]. Hence, doping $g\text{-C}_3\text{N}_4$ with transition and rare earth elements is a promising strategy for enriching photocatalytic activity under visible-light irradiation.

In the current research, we successfully impregnated lanthanum and cobalt oxides with $g\text{-C}_3\text{N}_4$ hydrothermally to fabricate $\text{La}_2\text{O}_3\text{-}g\text{-C}_3\text{N}_4$, $\text{CoO-}g\text{-C}_3\text{N}_4$, and $\text{La}_2\text{O}_3\text{-CoO-}g\text{-C}_3\text{N}_4$ nanocomposite as effective photocatalysts for photoelectrochemical water-splitting (PECWS) and photodegradation studies. The $\text{La}_2\text{O}_3\text{-CoO-}g\text{-C}_3\text{N}_4$ nanocomposite showed better PECWS performance, and it was characterized by XRD, FE-SEM, EDX, UV-VIS, FTIR for structural, morphological, and EDX elemental analysis. Photoelectrochemical measurements showed improved photocurrent generation in a standard three-electrode electrochemical cell using a neutral electrolyte and enhanced photocatalytic activities compared to the competing photocatalysts.

2. Experimental

2.1. Materials and Chemicals

Highly pure, analytical-grade materials such as chemicals, solvents, and reagents were purchased. Most of them were used in their original state without further purifications unless otherwise stated. Lanthanum (III) nitrate hexahydrate (99.99%), cobalt (II), nitrate hexahydrate (98%), sodium sulfate (99%), melamine (99%), ethanol, acetone, and methylene blue were purchased from Sigma Aldrich and used as received. Deionized water was used for all measurements and solutions or dilutions, including solutions used in photoelectro-

chemical (PEC) experiments. Fluorine-doped tin oxide (FTO) substrates of dimensions (length \times width \times thickness = 25 mm \times 25 mm \times 1.1 mm, resistivity = 7–15 Ω and transmittance > 80%) were purchased from redox.me through a local vendor. Before use, FTO substrates were ultrasonicated in ethanol and water for 15 min each, correspondingly.

2.2. Synthesis of g-C₃N₄

Melamine was used as starting precursor to prepare graphitic carbon nitride (g-C₃N₄). First, a known amount of melamine was annealed in the air within a muffle furnace for 5 h at 550 °C until a yellowish powder was obtained. In the next step, a physical transformation strategy with slight modification [44] yielded nanoflakes with the morphology of g-C₃N₄. Then, the bulk g-C₃N₄ powder obtained was exfoliated to attain g-C₃N₄ nanoflakes by probe sonication for 2 h in 70% ethanol solution. Finally, the as-prepared g-C₃N₄ nanoflakes were collected by centrifugation at 4000 rpm and vacuum dried at 120 °C for 2 h.

2.3. Synthesis of La₂O₃-g-C₃N₄, CoO-g-C₃N₄, and La₂O₃-CoO-g-C₃N₄ Nanocomposites

To prepare La₂O₃-g-C₃N₄, CoO-g-C₃N₄, and La₂O₃-CoO-g-C₃N₄ nanocomposites, a hydrothermal approach was followed. In the first step, aqueous solution mixtures of the precursors were prepared in the following order:

- (i) 50% by weight each of lanthanum (III) nitrate hexahydrate with g-C₃N₄ nanoflakes,
- (ii) 50% by weight each of cobalt (II) nitrate hexahydrate and g-C₃N₄ nanoflakes, and
- (iii) 25% by weight, each of lanthanum (III) nitrate hexahydrate and cobalt (II) nitrate hexahydrate solutions and 50% by weight of g-C₃N₄ nanoflakes solutions were prepared in deionized water.

Each reaction mixture was sonicated for 30 min. The three precursor solutions were then mixed, with further sonication for 60 min to achieve homogenization. In the second step, each reaction mixture containing the nitrate salts of La, Co, and g-C₃N₄ nanoflakes was transferred into a separate stainless-steel autoclave containing PPL-lined vessels. The hydrothermal reaction was carried out for 24 h at 180 °C. Afterward, the reaction mixture was centrifuged at 4000 rpm for 5 min. Finally, the La₂O₃-g-C₃N₄, CoO-g-C₃N₄, and La₂O₃-CoO-g-C₃N₄ nanocomposites were collected and rinsed with deionized water and ethanol thrice prior to drying in a vacuum oven for 2 h at 150 °C. Finally, the La₂O₃-g-C₃N₄, CoO-g-C₃N₄, and La₂O₃-CoO-g-C₃N₄ nanocomposites were annealed at 550 °C for 4 h, and the powders were used for characterization, PEWS, and dye degradation experiments.

2.4. Characterization

All the nanomaterials for crystallinity and phase analysis were characterized by powder X-ray diffractometer by a SHIMADZU XRD-6100 instrument containing a Cu K α radiation source and operating at 60 kV/80 mA. The pure, g-C₃N₄, La₂O₃-g-C₃N₄, CoO-g-C₃N₄, and La₂O₃-CoO-g-C₃N₄ nanocomposites were studied with the X-ray diffraction (XRD) technique. XRD patterns were recorded in the range of 10–80° (2 θ) at a scanning rate of 5° min⁻¹. The structural composition and crystalline phases of La₂O₃-g-C₃N₄, CoO-g-C₃N₄, and La₂O₃-CoO-g-C₃N₄ nanocomposites were determined from the ICDD-PDF-2/PDF-4 library database. The structure and topology of the nanomaterials was observed under a TESCAN Lyra 3 field emission dual beam (electron/focused ion beam) aided by a high-end field-emission scanning electron microscope (FE-SEM) supported with EDX for structural composition and elemental speciation of La₂O₃-CoO-g-C₃N₄ nanocomposites. The optical properties of La₂O₃-CoO-g-C₃N₄ nanocomposites were studied by measuring their absorbance on a Jenway 6850 double beam UV-VIS spectrophotometer with variable bandwidth. The vibrational spectroscopy was carried out using a Shimadzu IRAffinity-1s Fourier-Transform Infrared spectrophotometer (Shimadzu, Kyoto, Japan). The photoelectrochemical measurements were performed on an Electrochemical workstation from IVIUM-n-stat having a multichannel specification for electrochemical analysis. For photocatalysis, 1 sun irradiation was achieved by ABET 10,500 Solar simulator follow-

ing ASTM, IEC, and JIS Class A standards and providing an AM 1.5G output using a DC Xenon Arc Lamp (Thorlabs, Newton, NJ, USA) and a UV cutoff filter.

2.5. Photoelectrochemical Measurements and Setup

For photoelectrochemical measurements, FTO substrates were coated with pristine g-C₃N₄, La₂O₃-g-C₃N₄, CoO-g-C₃N₄, and La₂O₃-CoO-g-C₃N₄ nanocomposites. FTO glass substrates were washed thoroughly with deionized water and ultrasonicated in acetone for 10 min. In the subsequent step, the photoanodes were prepared. The slurries of each g-C₃N₄, La₂O₃-g-C₃N₄, CoO-g-C₃N₄, and La₂O₃-CoO-g-C₃N₄ nanomaterials were mixed in 50% (v/v) ethanol/water, then 20 µL of 5% Nafion solution was added, and the final mixture of each slurry was drop-casted on the respective pre-treated FTO substrates. The coated FTO/g-C₃N₄ and FTO/La₂O₃-g-C₃N₄, FTO/CoO-g-C₃N₄, and FTO/La₂O₃-CoO-g-C₃N₄ photoanodes were heated at 110 °C for 2 h to evaporate the solvents and harden the films. PEC measurements were carried out in 0.5 M Na₂SO₄ solution (pH = 7) using a tri-electrode electrochemical setup comprising FTO/g-C₃N₄ and FTO/La₂O₃-g-C₃N₄, FTO/CoO-g-C₃N₄, and FTO/La₂O₃-CoO-g-C₃N₄ photoanode substrates used as working electrodes, a Pt wire as the auxiliary electrode, and a standard Ag/AgCl as the reference electrode. PEC experiments were accomplished with an IVIUM-n-stat multichannel electrochemical workstation (Ivium Technologies BV, Eindhoven, The Netherlands). For photocatalysis experiments, 1 sun irradiation was achieved by using an ABET 10,500 Solar simulator (ASTM, IEC, and JIS Class A certified) (Abet Technologies, Milford, CT, USA), having a DC Xenon Arc lamp (Thorlabs, Newton, NJ, USA), an Air Mass 1.5G filter, and a 35 mm field diameter aperture for outputting 1 sun beam with a UV cutoff filter.

2.6. Photocatalytic Dye Degradation Studies

For photocatalytic degradation studies of pristine g-C₃N₄, La₂O₃-g-C₃N₄, CoO-g-C₃N₄, and La₂O₃-CoO-g-C₃N₄ nanocomposites, 5 ppm methylene blue (MB) aqueous solution was prepared. For each experimental batch, 10 mg of photocatalyst was loaded into 20 mL of MB, with continuous stirring in the dark for 20 min. Later, the MB solution was exposed to 1 sun visible light for 40 min through an Ozone-free Xe Arc Lamp (150 W) (Thorlabs, Newton, NJ, USA) solar simulator. Afterward, centrifugation of the visible-light-treated reaction mixture at 6000 rpm for 10 min was carried out. The absorbance of the supernatant was recorded by a Jenway 6850 double-beam UV-VIS spectrophotometer (Cole-Parmer Ltd., Eaton Socon, UK). Steps similar to the ones mentioned above were repeated until maximum photodegradation was achieved by each photocatalyst.

3. Results and Discussion

3.1. X-ray Diffraction (XRD) Analysis

The crystalline properties of pristine-g-C₃N₄, La₂O₃-g-C₃N₄, CoO-g-C₃N₄, and La₂O₃-CoO-g-C₃N₄ nanomaterials were investigated by XRD analysis, as presented in Figure 1. The XRD patterns disclose the characteristic diffraction peaks of g-C₃N₄ nanoflakes, cobalt oxide, and lanthanum oxide, labeled by the specific *hkl* values, respectively. The XRD pattern of g-C₃N₄ nanoflakes showed characteristic diffraction peaks at 2θ values observed at 13° and 27° corresponding to *hkl* Miller indices of (100) and (002), which are well aligned with JCPDS card number 87-1526 [39]. Furthermore, it is evident that in each La₂O₃-g-C₃N₄ and La₂O₃-CoO-g-C₃N₄, the 2θ peak of g-C₃N₄ observed at 13° with *hkl* value of (100) disappeared a bit whereas the 2θ° peak at 27°, and *hkl* miller indices of (002) merged with characteristic peaks of La₂O₃ oxide. However, in CoO-g-C₃N₄, a sole and distinguishable peak of g-C₃N₄ of 2θ° values at 27° corresponding to *hkl* Miller index (002) was observed but 2θ° peak at 13° to *hkl* planes of (100) disappeared. Hence, the formation of nanocomposite materials where metals La and Co were impregnated with triazine structures of g-C₃N₄ by the hydrothermal reaction was confirmed in the respective nanomaterials. In the XRD patterns of both CoO-g-C₃N₄ and La₂O₃-CoO-g-C₃N₄ nanomaterials, some common

diffraction peaks at 2θ values of 21.5° , 32.7° , 38.1° , and 45.1° correspond to the hkl lattice planes (111), (220), (311), and (222) were observed that support the existence of cobalt oxide “CoO” in the $\text{La}_2\text{O}_3\text{-CoO-g-C}_3\text{N}_4$ nanocomposite. However, some additional peaks of CoO were also found in $\text{La}_2\text{O}_3\text{-CoO-g-C}_3\text{N}_4$ with 2θ values of 49.6° , 59.4° , and 65.5° corresponding to the hkl lattice planes (422), (511), and (440), respectively. It is also worth mentioning that the intensity of CoO peaks in $\text{CoO-g-C}_3\text{N}_4$ was somewhat on the lower side as compared to CoO XRD peak intensity observed in $\text{La}_2\text{O}_3\text{-CoO-g-C}_3\text{N}_4$ nanocomposite. Thus, the predicted cobalt oxide phase was found to exist in the cubic crystalline structure with space group $\text{Fm}\bar{3}\text{m}$ and completely matched ICSD pattern 53057 [45,46] and JCPDS card No. 43-1003 [39] in $\text{CoO-g-C}_3\text{N}_4$ and $\text{La}_2\text{O}_3\text{-CoO-g-C}_3\text{N}_4$ nanomaterials, respectively. Figure 1 also describes the XRD pattern of $\text{La}_2\text{O}_3\text{-g-C}_3\text{N}_4$ and $\text{La}_2\text{O}_3\text{-CoO-g-C}_3\text{N}_4$ nanomaterials. The XRD diffraction peaks of lanthanum oxide “ La_2O_3 ” were significant in both materials. The $2\theta^\circ$ peaks observed at 15° , 27° , 28° , 39° , and 48° , respectively, corresponded to the hkl values of (101), (222), (300), (400), and (622), respectively. These X-ray diffraction peaks represent the dimensions of the nano-range particles. Furthermore, these diffraction data were well aligned with a cubic crystalline phase and lattice parameters according to the JCPDS card number 04-0856 [47]. The lattice parameters observed were $a = b = c = 11.420 \text{ \AA}$ and $\alpha = \beta = \gamma = 90^\circ$, respectively. The respective peaks of $\text{g-C}_3\text{N}_4$ were significantly recorded at $2\theta^\circ$ values of 27° , showing the successful formation of the composites. The CoO and La_2O_3 phases distinguishably shared some common reflections at 27° and 48° in the $\text{La}_2\text{O}_3\text{-CoO-g-C}_3\text{N}_4$ nanomaterial. In summary, the X-ray diffraction patterns of $\text{La}_2\text{O}_3\text{-CoO-g-C}_3\text{N}_4$ nanocomposite contained $\text{g-C}_3\text{N}_4$ characteristic peaks and showed La and Co oxide-specific peaks, which exhibited strong and sharp diffraction, corroborating high crystallinity. The diffraction peaks of $\text{La}_2\text{O}_3\text{-CoO-g-C}_3\text{N}_4$ were consistent with the standard patterns of cubic spinel cobalt oxide and lanthanum oxides, suggesting that they have a cubic phase structure in the $\text{La}_2\text{O}_3\text{-CoO-g-C}_3\text{N}_4$ nanocomposite. Furthermore, no additional diffraction peaks were found regardless of the variation in the peak’s intensity in pristine $\text{g-C}_3\text{N}_4$, $\text{La}_2\text{O}_3\text{-g-C}_3\text{N}_4$, $\text{CoO-g-C}_3\text{N}_4$, and $\text{La}_2\text{O}_3\text{-CoO-g-C}_3\text{N}_4$ nanomaterials. This indicates that hydrothermal and annealing methods for incorporating metal precursors and sonication efficiently resulted in nanocomposite formation.

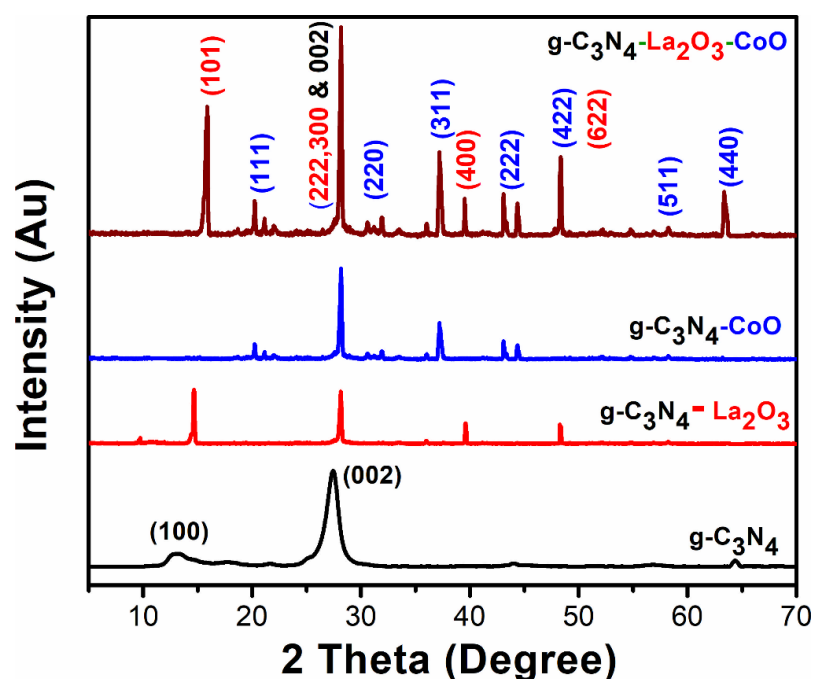


Figure 1. The XRD analysis of $\text{g-C}_3\text{N}_4$, $\text{g-C}_3\text{N}_4\text{-CoO}$, $\text{g-C}_3\text{N}_4\text{-La}_2\text{O}_3$, and $\text{La}_2\text{O}_3\text{-CoO-g-C}_3\text{N}_4$ Nanomaterials.

In the post-PEC sample analysis, we scratched the used $\text{La}_2\text{O}_3\text{-CoO-g-C}_3\text{N}_4$ photoanode and re-characterized it by XRD and FE-SEM/EDX. XRD analysis helped to investigate the stability and structural and compositional changes in the photocatalyst taking place during the photoelectrochemical process. The XRD pattern recorded is presented in Figure S1 (Supplementary Information). Multiple La oxide, hydroxide, and Co oxide phases were detected. In the post electrochemical XRD, it was evident that La_2O_3 , CoO, and g C_3N_4 peaks appeared significantly at their specified 2θ positions, as shown in Figure 1, which supports the stability of the $\text{La}_2\text{O}_3\text{-CoO-g-C}_3\text{N}_4$ photocatalyst. However, after the water-splitting process, some new peaks of low to moderate intensity were observed, which were distinguished by different colors for $\text{La}(\text{OH})_3$ and Co_3O_4 , respectively. This happened because of electrolyte interaction with the photocatalyst under visible light and electrochemical reactions. $\text{La}(\text{OH})_3$ can be recognized by its 2θ positions at 14.5° , 26.2° , 27.8° , 30° , 42° , 53.8° , and 71.4° . These 2θ values communicate hkl Miller indices from the reflections at (100), (110), (101), (200), (210), (112), and (302). This post-XRD pattern is well aligned with the standard JCPDS card number #36-1481 for hexagonal P63 $\text{La}(\text{OH})_3$. On the other hand, due to the PEWS process, some low-intensity XRD peaks from Co_3O_4 were also observed. These can be seen at 2θ values 10.8° , 15.8° , 17.2° , 24.1° , 30° , and 33.7° , respectively, in Supplementary Information. Their corresponding hkl Miller indices were (111), (220), (311), (331), (333), and (440). These peaks are in accordance with the JCPDS card number 01-078-1969, a cubic phase Co_3O_4 . In the XRD pattern of the post electrochemical measurement sample (Figure S1), high-intensity peaks of freshly prepared $\text{La}_2\text{O}_3\text{-CoO-g-C}_3\text{N}_4$ photocatalyst (Figure 1) can be seen evidently. It is worth noting that during the PEWS process, some of the La_2O_3 changed to $\text{La}(\text{OH})_3$ hexagonal phase, and CoO oxides transformed into cobalt oxide phases such as $\text{Co}^{(+2)}$ $\text{Co}^{(+3)}$ in Co_3O_4 . This is another reason for the enhanced PEWS activity of $\text{La}_2\text{O}_3\text{-CoO-g-C}_3\text{N}_4$ where mixed phases of La and valance states of cobalt metal such as Co^{2+} and Co^{3+} coexist. It is also due to the combined effect of the metal oxide's impregnation with g- C_3N_4 arising from the chemical coupling effects of La and Co oxides and with g- C_3N_4 support that led to efficient separation of the photogenerated charge carriers and enhanced the photocatalytic hydrogen production activity of the photocatalysts. Such behavior of Co oxides with g- C_3N_4 toward enhanced photocatalytic activity has been reported in the literature [48–50]. In summary, the differences in the XRD analysis (Figure S1) illustrate that the crystal structure of the $\text{La}_2\text{O}_3\text{-CoO-g-C}_3\text{N}_4$ photocatalysts did not change greatly even after the photocatalytic reaction. Therefore, $\text{La}_2\text{O}_3\text{-CoO-g-C}_3\text{N}_4$ can be regarded as a stable photocatalyst for photoelectrochemical water-splitting reactions.

3.2. Surface Morphology and EDX Analysis

The low- and high-resolution FE-SEM micrographs of $\text{La}_2\text{O}_3\text{-CoO-g-C}_3\text{N}_4$ are presented in Figure 2. Figure 2a,d depicts the nanoflake-like morphology of the g- C_3N_4 , whereas Figure 2b,e and Figure 2c,f depict the nanocomposite obtained by hydrothermal treatment of g- C_3N_4 with La and Co precursors. It is evident from the SEM images that the nanocomposite includes nanoflakes of g- C_3N_4 embedded with La_2O_3 and CoO nanoparticles. A range of different dimensions of $\text{La}_2\text{O}_3\text{-CoO}$ nanoparticles beyond 50 nm with clusters was observed in FE-SEM analysis, as seen in Figure 2e,f. Spongy agglomerations with different pores and voids were also observed. The reduction in the nanoparticle size beyond 50 nm suggested that lanthanum and cobalt atoms are well incorporated into the g- C_3N_4 triazine rings [48] without phase partition, thus, shaping the nanocomposite of $\text{La}_2\text{O}_3\text{-CoO-g-C}_3\text{N}_4$. Consequently, a complete transformation of the starting precursor into metal oxides [51,52] and impregnation in to the triazine structures of g- C_3N_4 was noted. It is more apparent from the EDX spectrum that the $\text{La}_2\text{O}_3/\text{CoO}$ nanoparticles were successfully infused with the g- C_3N_4 and appeared as major constituents of the nanocomposite. The EDX analysis further confirms the presence of La, Co, C, N, and O elements in good atomic ratios at their characteristic energy peaks and intensities. Likewise, the EDX spectrum presented in Figure 2g,h demonstrated specific elemental K(α) and L (α)

electronic transitions originated by the respective C, N, O, La, and Co elements from the $\text{La}_2\text{O}_3\text{-CoO-g-C}_3\text{N}_4$ crystalline phases. The elemental existence and cubic crystalline nature of the nanocomposite were also well aligned with the XRD findings.

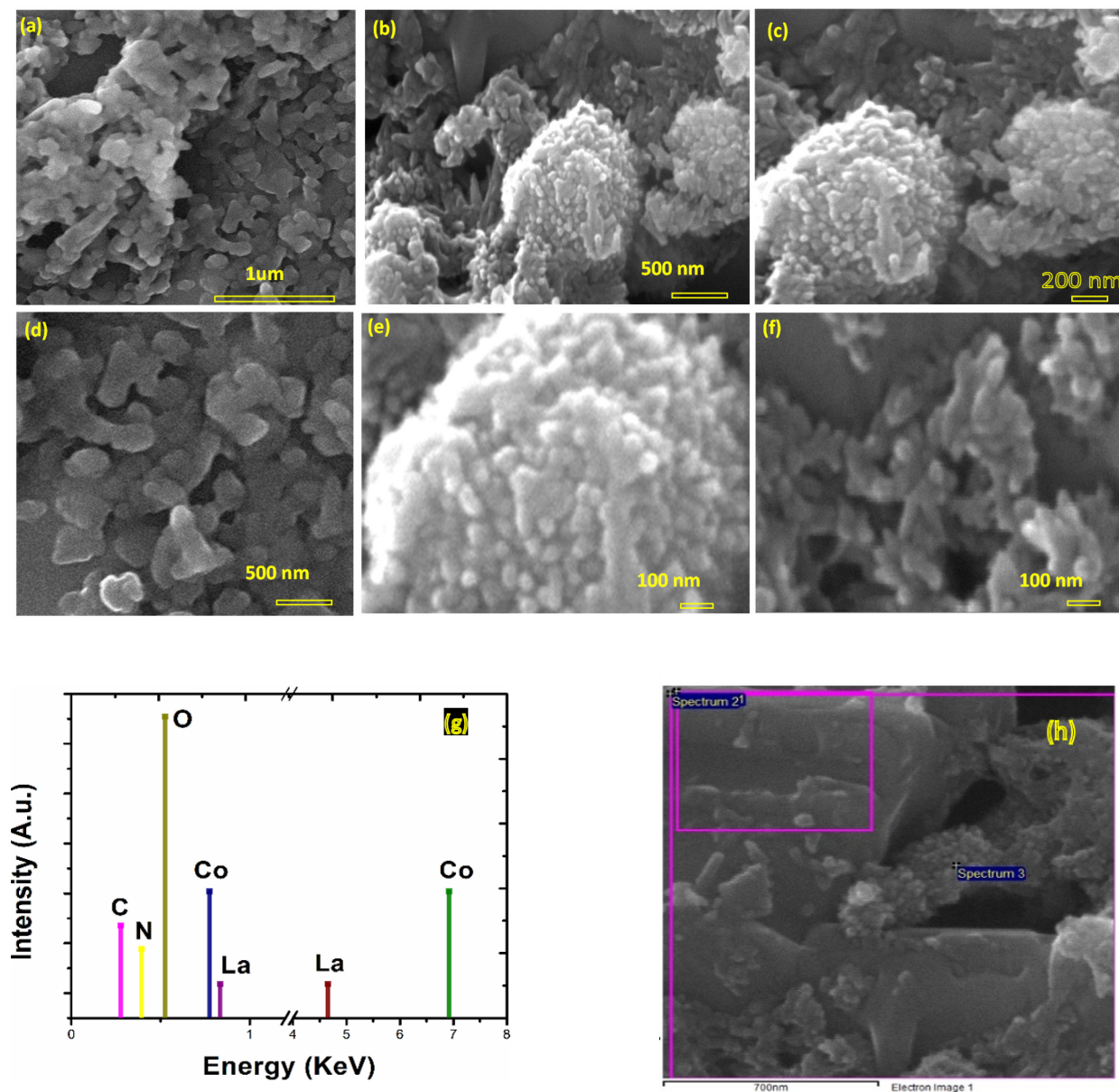


Figure 2. Low- and high-resolution SEM micrograph of $\text{g-C}_3\text{N}_4$ nanoflakes (a,d). High-resolution micrographs of $\text{La}_2\text{O}_3\text{-CoO-g-C}_3\text{N}_4$ nanocomposites showing nanoparticles clusters entrenched with $\text{g-C}_3\text{N}_4$ nanoflakes (b,e) and (c,f). EDX spectrum showing characteristic elemental peaks for K(α) and L (α) electronic transitions from respective C, N, O, La, and Co elements (g,h).

The post photoelectrochemical measurement FE-SEM analysis presented a comparative view of the surface topography of $\text{La}_2\text{O}_3\text{-CoO-g-C}_3\text{N}_4$ photocatalyst prepared hydrothermally. Figure S2a,b describes the agglomeration of La and Co oxide nanoparticles over the $\text{g-C}_3\text{N}_4$. The fresh sample as seen in Figure 2a,d comprised nanoflakes of $\text{g-C}_3\text{N}_4$, which after the water-splitting reaction were converted into thick flakes with chunks or agglomerations of La and Co oxide nanoparticles. The XRD data (Figure 1 and Figure S1) showed significant peaks of $\text{La}_2\text{O}_3\text{-CoO-g-C}_3\text{N}_4$ at its specified 2θ positions with comparable intensities in both pre- and post-PEC measurement samples, thus augmenting the stability of the $\text{La}_2\text{O}_3\text{-CoO-g-C}_3\text{N}_4$ photocatalyst. Furthermore, the EDX elemental

analysis of the used $\text{La}_2\text{O}_3\text{-CoO-g-C}_3\text{N}_4$ photocatalyst showed La, Co, O, N, and C elements at their known KeV values as described in Figure S2c,d of the Supplementary Information. The post-measurement EDX analysis was compared with the pre-analysis, and it was concluded that all the key elements with respect to energy/electronic transitions were present in good and comparable atomic intensities as well as being in close agreement with each other. Thus, $\text{La}_2\text{O}_3\text{-CoO-g-C}_3\text{N}_4$, even after the water-splitting process, retains the homogenous distribution of La and Co oxides on the surface. That resulted in enhanced PEWS activity.

3.3. UV-Visible Spectroscopy

The optical properties of the selected $\text{g-C}_3\text{N}_4$ nanoflakes and $\text{La}_2\text{O}_3\text{-CoO-g-C}_3\text{N}_4$ nanocomposites were probed by UV-VIS spectroscopy. To estimate the bandgap energy (E_g), we used absorbance data for Tauc plots [53–55]. Figure 3a,b presents the Tauc plots of $\text{g-C}_3\text{N}_4$ nanoflakes and $\text{La}_2\text{O}_3\text{-CoO-g-C}_3\text{N}_4$ nanocomposites, respectively. To find out the bandgap energy, $(\alpha h\nu)^2$ was plotted against the photon energy (eV). The bandgap energy was approximated from the energy curve. The spot where the coordinate on the lower energy side of the curve showed an exponential rise was considered for extrapolation. From that point, a straight line from the curve toward the x-axis gives the bandgap value of the material, as shown in Figure 3. The bandgap energy of pristine $\text{g-C}_3\text{N}_4$ and $\text{La}_2\text{O}_3\text{-CoO-g-C}_3\text{N}_4$ nanocomposites was estimated to be 2.7 and 2.38 eV, respectively. The interesting feature was the decrease in the bandgap of $\text{g-C}_3\text{N}_4$ on impregnation with La and Co oxides, which also resulted in greater photocatalytic properties.

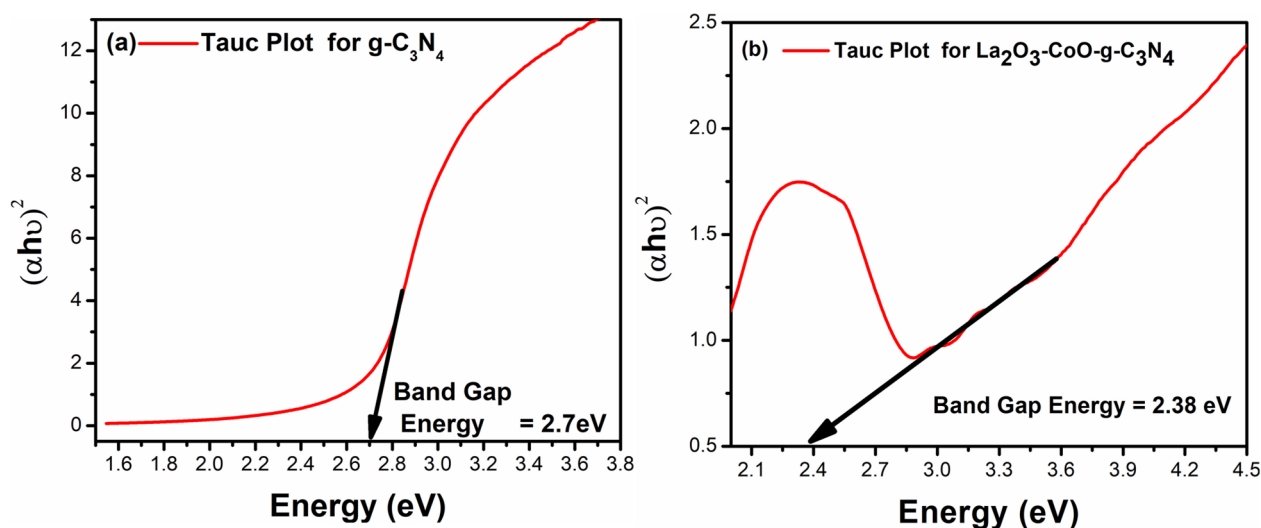


Figure 3. (a) Bandgap energy (E_g) calculations for $\text{g-C}_3\text{N}_4$ and (b) bandgap energy of $\text{La}_2\text{O}_3\text{-CoO-g-C}_3\text{N}_4$ nanocomposites calculated by UV-visible spectroscopy and employing the Tauc plot method.

3.4. FTIR Spectroscopy

FTIR analysis was performed in the wavenumber range from 400 to 4000 cm^{-1} . Figure 4a depicts the FTIR spectra of $\text{g-C}_3\text{N}_4$ nanoflakes, and Figure 4b presents the $\text{La}_2\text{O}_3\text{-CoO-g-C}_3\text{N}_4$ nanocomposite. The existence of triazine-based $\text{g-C}_3\text{N}_4$ nanoflakes was confirmed by the appearance of characteristics heterocyclic $\nu(\text{C-N/C=N})$ stretching vibrations and $\nu(\text{N-H})$ shearing vibrations bands from 1450 to 1650 cm^{-1} . The distinctive vibrational $\nu(\text{C-N/C=N})$ bands of abridged triazine units appeared at 1250, 1313, and 1391 cm^{-1} , which are ascribed to stretching vibrations of C-NH-C , i.e., partially condensed, and C-N(-C)-C , i.e., fully condensed units, respectively. A strong peak at 800 cm^{-1} matched the characteristic breathing mode vibrations of triazine units, which additionally confirms the formation of the $\text{g-C}_3\text{N}_4$ structure, as demonstrated in Figure 4a. These peak assignments are in agreement with the relevant literature [56–59]. On the other hand, a slight shift in

these vibrational peaks was observed when the g-C₃N₄ nanoflakes were hydrothermally impregnated with La and Co precursors to synthesize the La₂O₃-CoO-g-C₃N₄ nanocomposite. In Figure 4b, the FTIR spectra of the nanocomposite showed all the characteristics peaks for La₂O₃, CoO, and g-C₃N₄ nanocomposite. Significant differences in the FTIR spectra of g-C₃N₄ nanoflakes and La₂O₃-CoO-g-C₃N₄ nanocomposite were observed. The slight peak shifts and intensity change at 1195, 1374, 1435, 1530, 1656, and 3209 cm⁻¹, correspond to stretching and scissoring vibrations of -NH/-NH₂ groups [56–59]. These changes in the FTIR analysis of g-C₃N₄ nanoflakes and La₂O₃-CoO-g-C₃N₄ nanocomposite were credited to the impregnation of La₂O₃ and CoO nanoparticles with g-C₃N₄, which results in strong metal coordination with g-C₃N₄ nanoflakes. The medium to strong absorption bands at 643 cm⁻¹ were because of La-O stretching [47]. Simultaneously, Co-O stretching vibrations were recorded around 921 and 1020 cm⁻¹ [45,51]. Hence, the bands mentioned above confirm the presence of La₂O₃ and CoO in the La₂O₃-CoO-g-C₃N₄ nanocomposite. Furthermore, some broad transmittance peaks observed in the range of 3000–3300 cm⁻¹ were recognized as N-H vibrations, i.e., ν(N-H) stretching. The existence of a ν(N-H) band in the La₂O₃-CoO-g-C₃N₄ nanocomposite suggests that g-C₃N₄ nanoflakes remain protonated during hydrothermal impregnation of La and Co metal oxide nanoparticles, which also validates the stability of the triazine-based g-C₃N₄ structure. These interactions also influence and improve the photocatalytic properties of the catalyst to increase its performance.

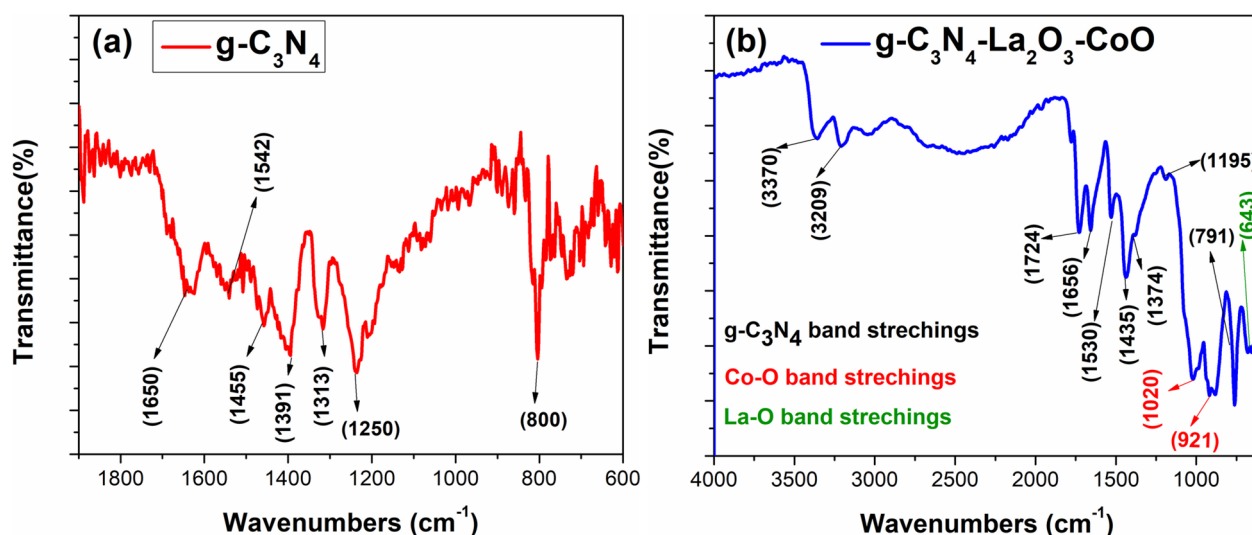


Figure 4. FTIR spectra of g-C₃N₄ (a) and La₂O₃-CoO-g-C₃N₄ (b).

3.5. Photoelectrochemical Measurements

Figure 5 shows the photoelectrochemical performance of pristine g-C₃N₄, La₂O₃-g-C₃N₄, CoO-g-C₃N₄, and La₂O₃-CoO-g-C₃N₄ nanocomposites in a standard three-electrode electrochemical cell using 0.5 M Na₂SO₄ electrolyte solution. The PEC measurements were performed under solar simulated 1 sun visible irradiation through UV cutoff and AMG 1.5 AM filters. The initial cyclic voltammograms (CVs) and linear sweep voltammetry (LSV) measurement experiments were performed on all the photocatalysts to investigate the photoelectrochemical activity. Figure 5a incorporates the CV curves of pristine g-C₃N₄, La₂O₃-g-C₃N₄, CoO-g-C₃N₄, and La₂O₃-CoO-g-C₃N₄ photoanodes. It is clearly seen that the CV response of the La₂O₃-CoO-g-C₃N₄ photoanode was 5, 4, and 3 folds higher than that of pristine g-C₃N₄, La₂O₃-g-C₃N₄, and CoO-g-C₃N₄ photoanodes, respectively. On the other hand, Figure 5b encompasses the LSV measurements carried out on g-C₃N₄, La₂O₃-g-C₃N₄, CoO-g-C₃N₄, and La₂O₃-CoO-g-C₃N₄ photoanodes with and without exposure to 1 sun light. In the dark mode, a negligible magnitude of photocatalytic reaction was observed. However, as the FTO-coated g-C₃N₄ electrode was exposed to 1 sun

light, an increase in photocurrent density ($250\mu\text{A}/\text{cm}^{-2}$) was observed from 0 to -1.5 V applied potential range. However, this current density was much lower as compared to the photocurrent generated by the FTO-coated $\text{La}_2\text{O}_3\text{-CoO-g-C}_3\text{N}_4$ nanocomposite. Similarly, the FTO-coated $\text{La}_2\text{O}_3\text{-g-C}_3\text{N}_4$ and $\text{CoO-g-C}_3\text{N}_4$ nanomaterials were also tested under 1 sun irradiation in the same voltage window. A similar trend of photoelectrochemical activity was observed, the photocurrent produced by $\text{La}_2\text{O}_3\text{-g-C}_3\text{N}_4$ was 2–3 times lower as compared to that for the $\text{La}_2\text{O}_3\text{-CoO-g-C}_3\text{N}_4$ photocatalyst; whereas the $\text{CoO-g-C}_3\text{N}_4$ photoanodes showed a twice higher response than that of the $\text{La}_2\text{O}_3\text{-g-C}_3\text{N}_4$ photoanode but significantly lower than that of $\text{La}_2\text{O}_3\text{-CoO-g-C}_3\text{N}_4$ photoanodes when exposed to 1 sun light. Upon comparing the photo current density of the FTO-coated $\text{La}_2\text{O}_3\text{-CoO-g-C}_3\text{N}_4$ nanocomposite, it was revealed that it generated a current density of $3.75\text{ mA}/\text{cm}^{-2}$ in the negative potential range, which depicts a reduction or hydrogen evolution reaction. However, the photocurrent densities observed from $\text{g-C}_3\text{N}_4$, $\text{La}_2\text{O}_3\text{-g-C}_3\text{N}_4$, and $\text{CoO-g-C}_3\text{N}_4$ were significantly lower than that of $\text{La}_2\text{O}_3\text{-CoO-g-C}_3\text{N}_4$ photoanodes. This increase in photocurrent density is ascribed to the synergistic effect of La and Co oxides impregnation within the $\text{g-C}_3\text{N}_4$ nanoflakes. The low photocurrent observed from $\text{g-C}_3\text{N}_4$, $\text{La}_2\text{O}_3\text{-g-C}_3\text{N}_4$, and $\text{CoO-g-C}_3\text{N}_4$ was due to reduced conversion efficiencies because of the rapid electron–hole recombination and simultaneous charge recombination, diminutive electrical conductivity, low optical absorption, and inadequate surface area for the photocatalytic reaction [30]. On the other hand, these limitations were resolved by La and Co doping in $\text{g-C}_3\text{N}_4$, which enhanced the photoelectrochemical recital of the $\text{g-C}_3\text{N}_4$ as reflected by the $\text{La}_2\text{O}_3\text{-CoO-g-C}_3\text{N}_4$ nanocomposite's response. These facts are also supported in the literature, whereby doping transition and rare earth metals [31–36] increased the photoelectrochemical performance of the materials. A similar trend of photocurrent response can be seen in the cyclic voltammograms (CVs) of $\text{g-C}_3\text{N}_4$ and $\text{La}_2\text{O}_3\text{-CoO-g-C}_3\text{N}_4$ nanocomposite in the light mode. Figure 5a incorporates the CV curves; when the 1 sun solar irradiation is on, a high current density was recorded beyond $3.5\text{ mA}/\text{cm}^{-2}$ by the $\text{La}_2\text{O}_3\text{-CoO-g-C}_3\text{N}_4$ nanocomposite but $\text{g-C}_3\text{N}_4$ significantly reduced the current density, here again, the aforementioned phenomena are playing their part.

Based on aforementioned observations, the chronoamperometry and impedance spectroscopy experiments were only performed on the pristine $\text{g-C}_3\text{N}_4$ and $\text{La}_2\text{O}_3\text{-CoO-g-C}_3\text{N}_4$ photoanodes. Figure 5c presents the chronoamperometry under chopped light, in ON and OFF mode for $\text{g-C}_3\text{N}_4$ and $\text{La}_2\text{O}_3\text{-CoO-g-C}_3\text{N}_4$ nanocomposite. The measurements were carried out at 0 V and open circuit potential (OCP). A substantial photocurrent response was observed when the FTO-coated $\text{La}_2\text{O}_3\text{-CoO-g-C}_3\text{N}_4$ electrode was exposed to 1 sunlight. On average, a $600\mu\text{A}/\text{cm}^{-2}$ photocurrent density was recorded from all the cycles under on/off mode during a significant period from the nanocomposite. The inset of Figure 5c shows the photocurrent density recorded by the $\text{g-C}_3\text{N}_4$ coated over the FTO electrode at OCP. The response was many folds decreased as compared to the photocurrent response monitored by the $\text{La}_2\text{O}_3\text{-CoO-g-C}_3\text{N}_4$ photoanode. It is known that photocatalytic response during water-splitting by carbon nitride suffers by fast charge recombination upon exposure to 1 sun simulated light [60]. This can be resolved by doping $\text{g-C}_3\text{N}_4$ with transition and rare earth metals. Therefore, $\text{La}_2\text{O}_3\text{-CoO-doped g-C}_3\text{N}_4$ nanocomposite engendered a high photocurrent response under 1 sun light accredited to La and Co hydrothermal impregnation that significantly improved the photocatalytic properties of $\text{g-C}_3\text{N}_4$. UV–VIS analysis and Tauc plots (Figure 3) also depicted the nanocomposite bandgap energy reduction. Thus, slow electron–hole charge recombination during a photocatalytic reaction was due to the high photocurrent density observed for the $\text{La}_2\text{O}_3\text{-CoO-g-C}_3\text{N}_4$ nanocomposite. As a result, an efficient photocatalyst was obtained with ample photocatalysis and renewable energy applications.

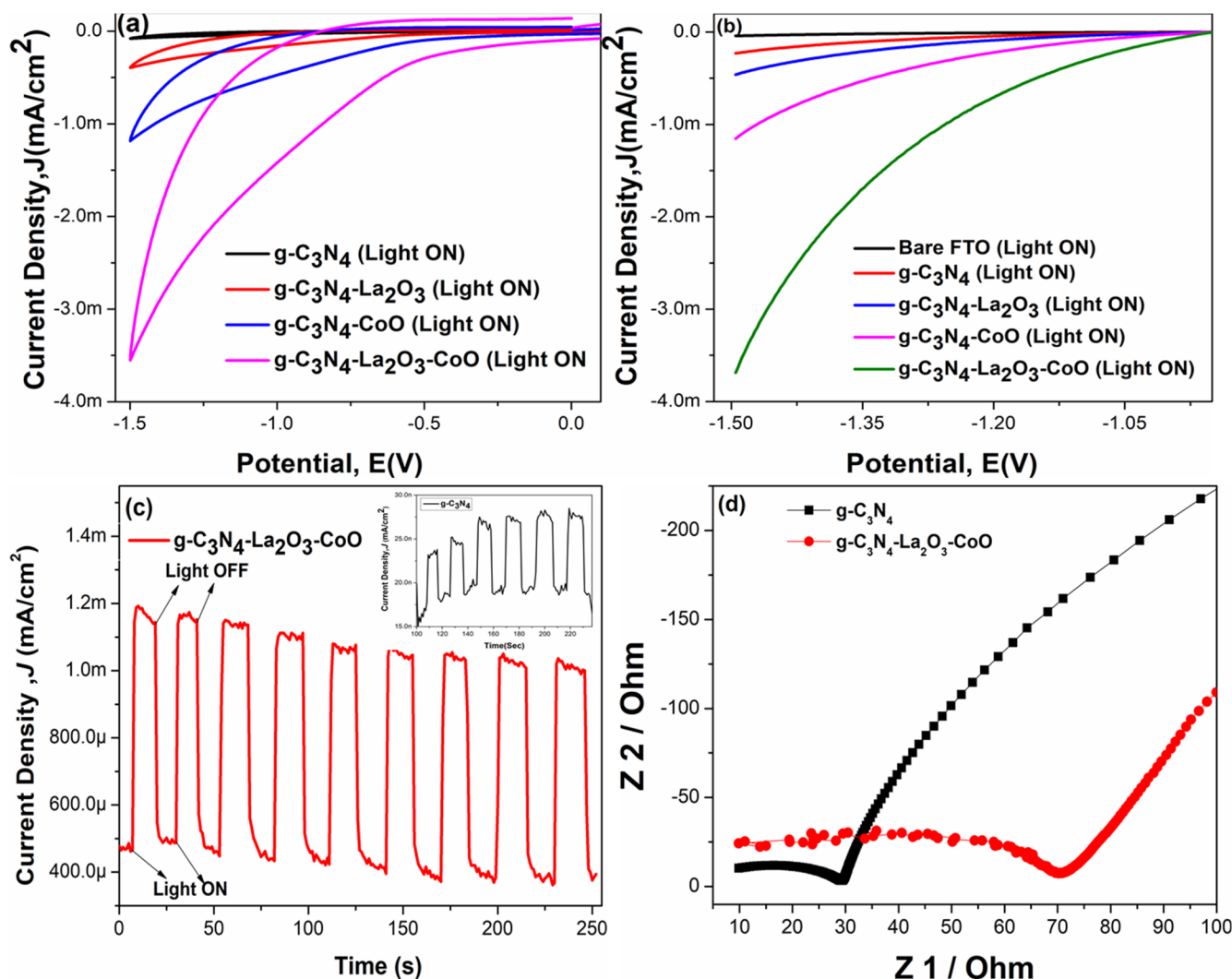


Figure 5. (a) Cyclic voltammetry of $g\text{-C}_3\text{N}_4$, $\text{La}_2\text{O}_3\text{-}g\text{-C}_3\text{N}_4$, $\text{CoO-}g\text{-C}_3\text{N}_4$, and $\text{La}_2\text{O}_3\text{-CoO-}g\text{-C}_3\text{N}_4$ nanocomposites. (b) Linear sweep voltammetry curves for $g\text{-C}_3\text{N}_4$, $\text{La}_2\text{O}_3\text{-}g\text{-C}_3\text{N}_4$, $\text{CoO-}g\text{-C}_3\text{N}_4$, and $\text{La}_2\text{O}_3\text{-CoO-}g\text{-C}_3\text{N}_4$ nanocomposites. (c) Chronoamperometry measurements of $g\text{-C}_3\text{N}_4$ and $\text{La}_2\text{O}_3\text{-CoO-}g\text{-C}_3\text{N}_4$ nanocomposite. (d) Impedance analysis of $g\text{-C}_3\text{N}_4$ and $\text{La}_2\text{O}_3\text{-CoO-}g\text{-C}_3\text{N}_4$ nanocomposite. All the photoelectrochemical measurements were conducted in a standard three-electrode cell with 0.5 M Na_2SO_4 solution, exposing the electrochemical cell to a 1 sun light irradiation source via a solar simulator.

Figure 5d presents the electrochemical impedance spectroscopy (EIS) for $g\text{-C}_3\text{N}_4$ and the $\text{La}_2\text{O}_3\text{-CoO-}g\text{-C}_3\text{N}_4$ nanocomposite. The EIS analysis assists in understanding the interfacial charge transfer kinetics. EIS also depicts the efficiency of obstructive recombination of photoinduced electron and hole pairs, in this case by $g\text{-C}_3\text{N}_4$ nanoflakes and $\text{La}_2\text{O}_3\text{-CoO-}g\text{-C}_3\text{N}_4$ nanocomposite, respectively. Figure 5d shows the Nyquist plot of $g\text{-C}_3\text{N}_4$ nanoflakes and $\text{La}_2\text{O}_3\text{-CoO-}g\text{-C}_3\text{N}_4$ nanocomposite. The semicircle's diameter was proportional to the charge-transfer resistance observed for the $\text{La}_2\text{O}_3\text{-CoO-}g\text{-C}_3\text{N}_4$ nanocomposite [61–63]. The $\text{La}_2\text{O}_3\text{-CoO-}g\text{-C}_3\text{N}_4$ nanocomposite had a lower charge transfer resistance (R_{ct}) and small arc radius, demonstrating the fast interfacial charge transfer efficiency compared to $g\text{-C}_3\text{N}_4$ in the Nyquist plot. This further supports fast electron transfer kinetics and effective separation of photogenerated electron and hole pairs by $\text{La}_2\text{O}_3\text{-CoO-}g\text{-C}_3\text{N}_4$ nanocomposite compared to $g\text{-C}_3\text{N}_4$. These EIS findings corroborated well with the greater photocatalytic activity of the $\text{La}_2\text{O}_3\text{-CoO-}g\text{-C}_3\text{N}_4$ nanocomposite compared to that of $g\text{-C}_3\text{N}_4$ as presented in Figure 5a–c. The incorporation of La and Co

oxides in the $g\text{-C}_3\text{N}_4$ was responsible for the significant increase in PEC performance, ultimately credited to photogenerated carriers in by La and Co oxides with higher separation efficiency compared to $g\text{-C}_3\text{N}_4$.

3.6. Methylene Blue Photodegradation Studies

To investigate the photocatalytic activity of $g\text{-C}_3\text{N}_4$, $\text{La}_2\text{O}_3\text{-}g\text{-C}_3\text{N}_4$, $\text{CoO-}g\text{-C}_3\text{N}_4$, and $\text{La}_2\text{O}_3\text{-CoO-}g\text{-C}_3\text{N}_4$ nanocomposites and a possible estimation of reaction kinetics of $\text{La}_2\text{O}_3\text{-CoO-}g\text{-C}_3\text{N}_4$ photocatalyst, photodegradation studies were performed using 5 ppm methylene blue (MB) aqueous solution. Before turning on the light for photocatalytic degradation, the adsorption–desorption equilibrium between MB and each photocatalyst was established by stirring 10 mg of photocatalyst in the MB mixture under dark for 20 min. The MB solution was exposed to 1 sun visible light for 40 min through an Ozone-free Xe Arc Lamp (150 W) (Thorlabs, Newton, NJ, USA) solar simulator. The photo decomposed reaction mixture was centrifuged at 6000 rpm for 10 min after every step before recording absorbance. Figure 6a,b shows the absorbance profile recorded after every 40 min for $g\text{-C}_3\text{N}_4$, $\text{La}_2\text{O}_3\text{-}g\text{-C}_3\text{N}_4$, $\text{CoO-}g\text{-C}_3\text{N}_4$, and $\text{La}_2\text{O}_3\text{-CoO-}g\text{-C}_3\text{N}_4$ nanocomposites. It is evident that the absorbance was decreasing as the exposure to visible light and the photocatalyst loading were increasing. This behavior was very significant for $\text{La}_2\text{O}_3\text{-CoO-}g\text{-C}_3\text{N}_4$ but for $g\text{-C}_3\text{N}_4$ and $\text{La}_2\text{O}_3\text{-}g\text{-C}_3\text{N}_4$ it was significantly lower. However, the photodegradation pattern of $\text{CoO-}g\text{-C}_3\text{N}_4$ was better than that of $g\text{-C}_3\text{N}_4$ and $\text{La}_2\text{O}_3\text{-}g\text{-C}_3\text{N}_4$ but still much lower comparing to $\text{La}_2\text{O}_3\text{-CoO-}g\text{-C}_3\text{N}_4$ photocatalyst. Therefore, further photodegradation studies were carried out for the $\text{La}_2\text{O}_3\text{-CoO-}g\text{-C}_3\text{N}_4$ photocatalyst.

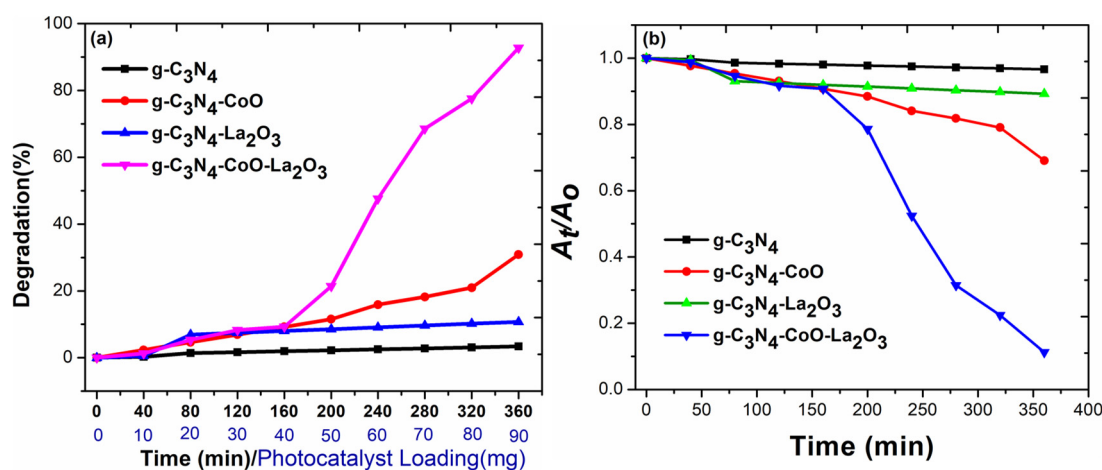


Figure 6. Photocatalytic degradation studies performed in 5 ppm methylene blue for $g\text{-C}_3\text{N}_4$, $\text{La}_2\text{O}_3\text{-}g\text{-C}_3\text{N}_4$, $\text{CoO-}g\text{-C}_3\text{N}_4$, and $\text{La}_2\text{O}_3\text{-CoO-}g\text{-C}_3\text{N}_4$ nanocomposites, (a) % photodegradation vs. light exposure time and photocatalyst loading, (b) absorbance efficiency of MB upon addition of 10 mg each photocatalyst vs. time of visible-light exposure.

Figure 7a depicts the absorbance curves at 0 min, showing that the measurement was performed without any catalyst and visible-light exposure. The subsequent measurements showed an increased rate of MB degradation, decolorization, and decreased absorbance until photodegradation was recorded beyond 90%. Methylene blue's (MB's) rate of photodegradation is measured by the following equation [64]:

$$\text{Degradation (\%)} = \left(\frac{A_0 - A}{A_0} \right) \times 100 \quad (1)$$

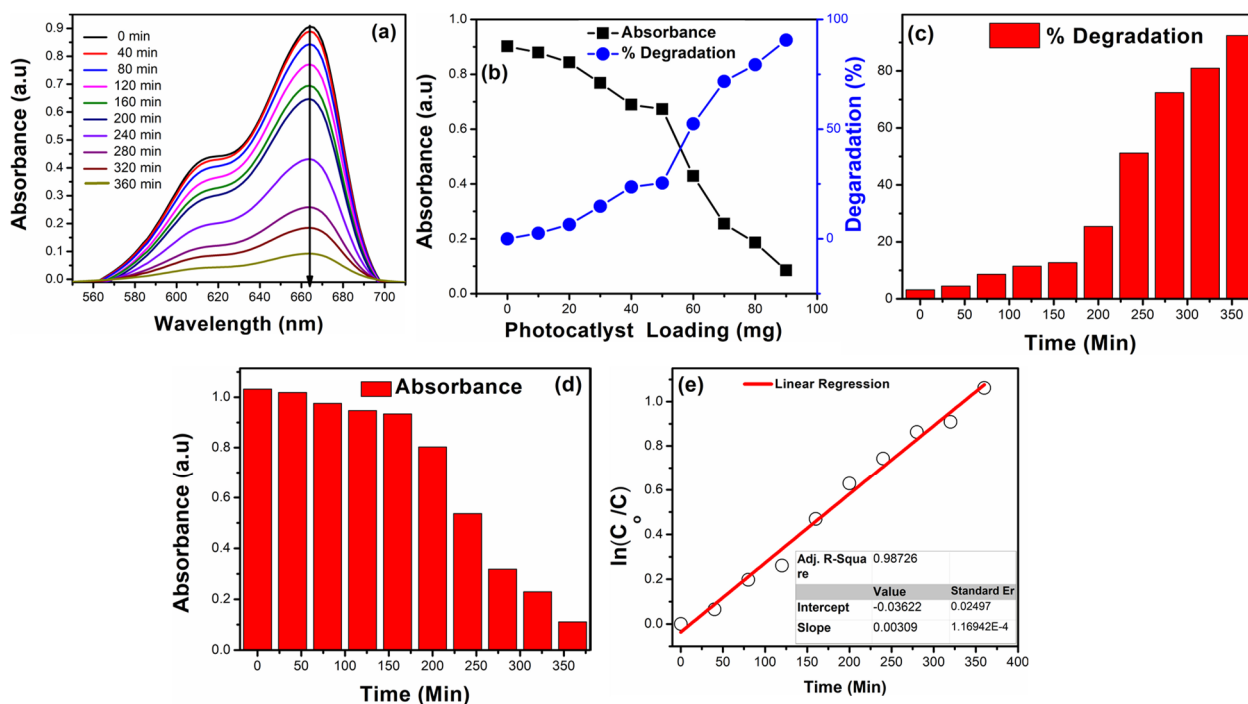


Figure 7. Dye photodegradation studies performed in 5 ppm methylene blue (MB) solution and by monitoring UV-absorption curves after every 40 min interval under 1 sun visible light. In each step, 10 mg $\text{La}_2\text{O}_3\text{-CoO-g-C}_3\text{N}_4$ nanocomposite was added to MB. (a) Photodegradation pattern of MB vs. time of exposure to 1 sun visible light. (b) Absorbance and % degradation profiles upon loading photocatalyst. (c) Degradation pattern of MB with respect to time. (d) Absorbance profile of MB upon addition of each increment of 10 mg $\text{La}_2\text{O}_3\text{-CoO-g-C}_3\text{N}_4$ nanocomposite vs. time of visible light exposure. (e) Linear regression analysis shows a pseudo-first-order reaction on the surface of the $\text{La}_2\text{O}_3\text{-CoO-g-C}_3\text{N}_4$ nanocomposite upon interaction with MB and visible light.

In the above equation, A_0 is the initial absorbance of MB solution, and A is the absorbance of the MB solution measured after exposure to visible light at time t .

Figure 7b–d presents the increase in photodegradation rate and decrease in MB solution absorbance with the increase in photocatalyst loading and time. These observations can be justified both in terms of the availability of active sites and penetration of visible light within nanocomposite structure, which enhances the reaction rate on the $\text{La}_2\text{O}_3\text{-CoO-g-C}_3\text{N}_4$ photocatalyst surface [65]. As the quantity of the photocatalysts increases, the deactivation of activated molecules by collision with ground state photocatalysts reduces its further interactions. At this stage, photodegradation of MB can reach its highest level where further addition of the photocatalyst will not make any appreciable difference in absorbance or photodegradation.

The reaction kinetics of an adsorption process delivers information about the mechanism of adsorption. The pseudo-first-order kinetic equation given by the Langmuir–Hinshelwood model at low initial concentrations [66] ensued. The photodegradation reaction of 5 ppm MB by $\text{La}_2\text{O}_3\text{-CoO-g-C}_3\text{N}_4$ photocatalyst follows a pseudo-first-order reaction kinetics. The photodegradation rate constant for the photodegradation reaction is determined from the equation below [67]:

$$\ln\left(\frac{C_0}{C}\right) = -kt \quad (2)$$

C_0 is the initial concentration, and C is the concentration at a particular time interval t during the irradiation, and k is the rate constant. Apparently, the rate of reaction in this study is believed to be the pseudo-first-order reaction. A plot of $\ln C_0/C$ versus time exemplified a straight line, as shown in Figure 7d. From the graphs, it was realized that the

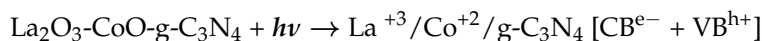
photocatalytic degradation of MB follows the first-order kinetics. The correlation constant observed from the fitted line was $R^2 = 0.98726$, which is considered a good correlation for the first-order reaction kinetics. The pseudo-first-order rate constant k was determined by the slope employing a linear regression. The rate constant observed for this reaction was 0.00309 min^{-1} for the $\text{La}_2\text{O}_3\text{-CoO-g-C}_3\text{N}_4$ nanocomposite.

The enhanced photodegradation performance of $\text{La}_2\text{O}_3\text{-CoO-g-C}_3\text{N}_4$ nanocomposite in MB is attributed to $\pi\text{-}\pi$ interactions and large surface area [68] provided synergistically by La_2O_3 and CoO nanoparticle in the $\text{g-C}_3\text{N}_4$ nanoflakes. However, these interactions are restricted in $\text{g-C}_3\text{N}_4$, $\text{La}_2\text{O}_3\text{-g-C}_3\text{N}_4$, and $\text{CoO-g-C}_3\text{N}_4$ nanocomposites, which can be due poor optical properties, lower surface area, decreased charge conversion efficiencies, and fast electron-hole and charge recombination in addition to weak electrical properties [30]. The characteristic absorbance maxima of MB was recorded at $\sim 664 \text{ nm}$ continuously due to its aromatic ring structures. Over time, the reaction mixture became colorless due to the breaking of those aromatic rings. Furthermore, photodegradation of MB under visible light irradiation also depends on the separation efficiency of electrons and holes [68]. It was evident from PEC and EIS measurements, as seen in Figure 5a–d, that $\text{La}_2\text{O}_3\text{-CoO-g-C}_3\text{N}_4$ nanocomposite recorded greater photocurrent generation following a hydrogen evolution reaction under visible light. Thus, high dye photodegradation under visible light is also ascribed to $\text{La}_2\text{O}_3\text{-CoO-g-C}_3\text{N}_4$ inhibition of photoexcited electron and hole recombination.

The mechanism of MB photodegradation can be explained by its conversion into innocuous substances such as $\text{CO}_2(\text{g})$, nitrates, ammonium, and sulfate ions, etc. A general scheme [67] of photocatalytic degradation of organic dyes is illustrated below, and Figure 8 represents a probable photocatalysis and dye photodegradation mechanism.

- Photon's absorption:

$$(h\nu \geq \text{band energy} = 2.38 \text{ eV for } \text{La}_2\text{O}_3\text{-CoO-g-C}_3\text{N}_4)$$



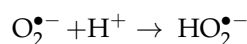
- Ionosorption of oxygen to $\text{O}_2^{\bullet-}$:



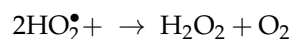
- Neutralization of OH^- groups and OH^\bullet radical formation by photoholes



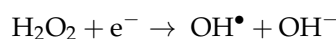
- $\text{O}_2^{\bullet-}$ neutralization of by protons:



- Dismutation of oxygen with transient hydrogen peroxide formation:



- The disintegration of H_2O_2 and subsequent oxygen reduction:



- Oxidation of the organic reactant of MB by OH^\bullet radicals:



- Direct oxidation by reaction with holes to generate degradation products

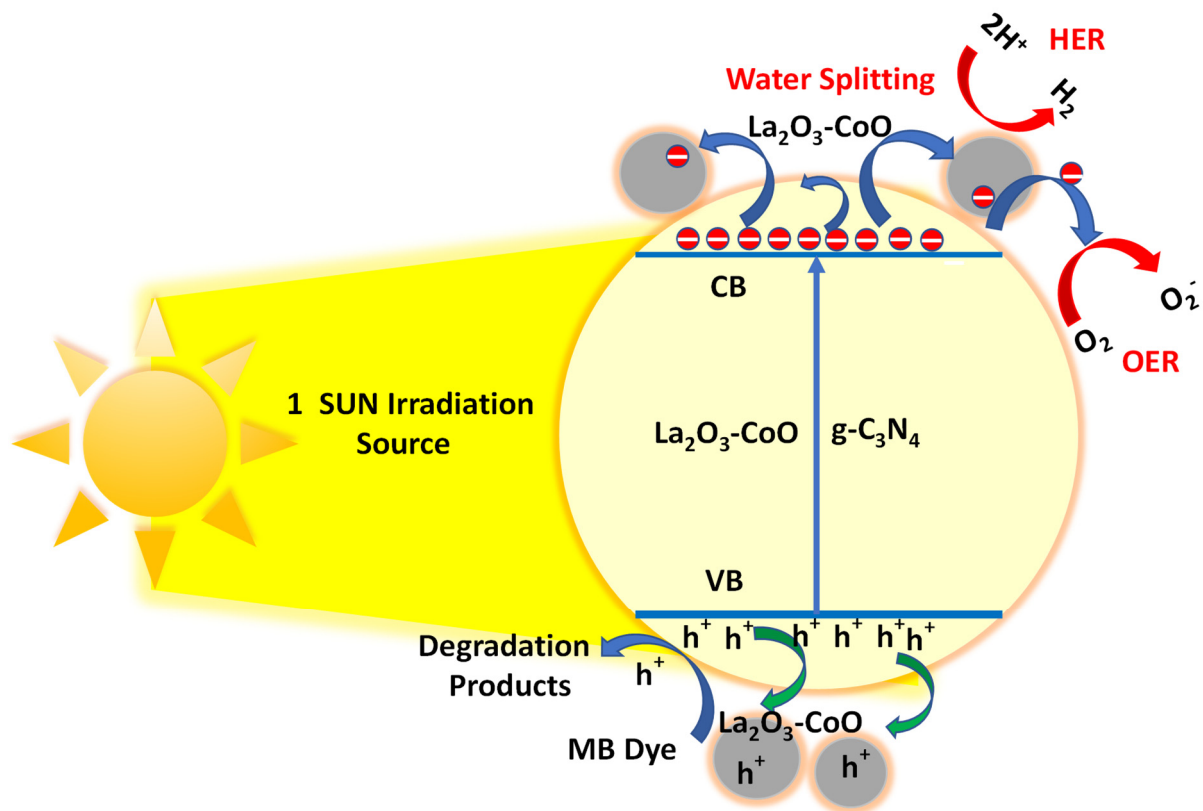
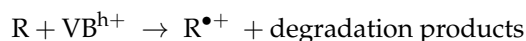


Figure 8. Pictorial illustration of a charge-transfer mechanism for photoelectrochemical water-splitting and MB photodegradation studies performed under 1 sun visible light.

4. Conclusions

A straightforward thermal/hydrothermal route is presented in the current research to synthesize $\text{La}_2\text{O}_3\text{-g-C}_3\text{N}_4$, $\text{CoO-g-C}_3\text{N}_4$, and $\text{La}_2\text{O}_3\text{-CoO-g-C}_3\text{N}_4$ from La, Co, and $\text{g-C}_3\text{N}_4$ precursors. $\text{La}_2\text{O}_3\text{-CoO-g-C}_3\text{N}_4$ is used as a photocatalyst and examined for photocatalytic water-splitting and MB photodegradation. The XRD analysis of $\text{La}_2\text{O}_3\text{-CoO-g-C}_3\text{N}_4$ nanocomposite supports the impregnation of $\text{La}_2\text{O}_3\text{-CoO}$ into $\text{g-C}_3\text{N}_4$ nanoflakes during the hydrothermal reaction and further corroborates its crystalline cubic structure. The microscopic investigations uncovered $\text{g-C}_3\text{N}_4$ nanoflakes' and $\text{La}_2\text{O}_3\text{CoO}$ nanoparticles' morphology within the $\text{La}_2\text{O}_3\text{-CoO-g-C}_3\text{N}_4$ nanocomposite, which offered a large surface area that improved photocatalytic reactions occurring on the surface of the photocatalyst. The EDX analysis confirmed characteristic elemental peaks from C, N, O, La, and Co elements in good agreement to the atomic ratios and their respective $K(\alpha)$ and $L(\alpha)$ electronic transitions. Bandgap energy (E_g) of 2.38 eV was calculated using the Tauc Plot method for $\text{La}_2\text{O}_3\text{-CoO-g-C}_3\text{N}_4$, which is reduced from $\text{g-C}_3\text{N}_4$ bandgap energy ($E_g = 2.7$ eV). The PEWS studies showed that due to the synergistic effect of $\text{g-C}_3\text{N}_4$, La_2O_3 and CoO impregnation, efficient separation of the photogenerated charge carriers, hydrogen evolution, and enhanced photocurrent efficiency (~ 3.75 mA/cm²) were recorded by $\text{La}_2\text{O}_3\text{-CoO-g-C}_3\text{N}_4$ as compared to $\text{g-C}_3\text{N}_4$, $\text{La}_2\text{O}_3\text{-g-C}_3\text{N}_4$, and $\text{CoO-g-C}_3\text{N}_4$ under visible-light irradiation in 0.5 M Na_2SO_4 electrolyte solution. The photocatalytic characteristics of $\text{g-C}_3\text{N}_4$, $\text{La}_2\text{O}_3\text{-g-C}_3\text{N}_4$, $\text{CoO-g-C}_3\text{N}_4$, and $\text{La}_2\text{O}_3\text{-CoO-g-C}_3\text{N}_4$ were further explored by MB photodegradation. Beyond 90% photodecomposition of MB with a continuous decrease in absorbance was monitored. The kinetic studies report a pseudo-first-order

reaction (where $k = 0.00309 \text{ min}^{-1}$) under 1 sun visible-light irradiation. The XRD, FE-SEM/EDX for post-PEWS samples of $\text{La}_2\text{O}_3\text{-CoO-g-C}_3\text{N}_4$ showed significant stability with similar crystalline phases and elemental composition as observed for freshly prepared samples. Thus, the hydrothermally anchored $\text{La}_2\text{O}_3\text{-CoO}$ with $\text{g-C}_3\text{N}_4$ photocatalyst has potential implementations in photocatalysis, environmental remediation, battery science, and renewable energy research areas.

Supplementary Materials: The following supporting information can be downloaded at: <https://www.mdpi.com/article/10.3390/catal12010015/s1>. Figure S1. The Post PEC measurements XRD spectrum of $\text{La}_2\text{O}_3\text{-CoO-g-C}_3\text{N}_4$. Figure S2. The surface morphology in post-PEC measurements of $\text{La}_2\text{O}_3\text{-CoO-g-C}_3\text{N}_4$ (a,b). (c,d) shows the EDX spectrum and corresponding micrograph.

Funding: Research group project number 0010-1443-S by Deanship of Scientific Research, University of Hafr Al Batin, Hafr Al Batin, Saudi Arabia.

Institutional Review Board Statement: Not applicable.

Informed Consent Statement: Not applicable.

Data Availability Statement: Not applicable.

Acknowledgments: The author extends appreciation to the Deanship of Scientific Research, University of Hafr Al Batin, for funding this work through the research group project number 0010-1443-S.

Conflicts of Interest: The author declares no conflict of interest in this study's design; in the collection, analyses, or interpretation of data; in the writing of the manuscript; or in the decision to publish the results.

References

1. Che, H.; Ngaw, C.K.; Hu, P.; Wang, J.; Li, Y.; Wang, X.; Teng, W. Fabrication of molybdenum doped carbon nitride nanosheets for efficiently photocatalytic water splitting. *J. Alloy. Compd.* **2020**, *849*, 156440. [CrossRef]
2. Guo, C.; Tian, K.; Wang, L.; Liang, F.; Wang, F.; Chen, D.; Ning, J.; Zhong, Y.; Hu, Y. Approach of fermi level and electron-trap level in cadmium sulfide nanorods via molybdenum doping with enhanced carrier separation for boosted photocatalytic hydrogen production. *J. Colloid Interface Sci.* **2021**, *583*, 661–671. [CrossRef]
3. Guo, C.; Li, L.; Chen, F.; Ning, J.; Zhong, Y.; Hu, Y. One-step phosphorization preparation of gradient-P-doped CdS/CoP hybrid nanorods having multiple channel charge separation for photocatalytic reduction of water. *J. Colloid Interface Sci.* **2021**, *596*, 431–441. [CrossRef]
4. Navarro Yerga, R.M.; Alvarez-Galván, M.C.; Vaquero, F.; Arenales, J.; Fierro, J.L.G. Chapter 3-Hydrogen Production from Water Splitting Using Photo-Semiconductor Catalysts. In *Renewable Hydrogen Technologies*; Gandía, L.M., Arzamendi, G., Diéguez, P.M., Eds.; Elsevier: Amsterdam, The Netherlands, 2013; pp. 43–61.
5. Sivula, K.; van de Krol, R. Semiconducting materials for photoelectrochemical energy conversion. *Nat. Rev. Mater.* **2016**, *1*, 15010. [CrossRef]
6. Han, H.S.; Park, W.; Sivanantham, A.; Hwang, S.W.; Surendran, S.; Sim, U.; Cho, I.S. Facile fabrication of nanotubular heterostructure for enhanced photoelectrochemical performance. *Ceram. Int.* **2021**, *47*, 3972–3977. [CrossRef]
7. Sim, Y.; John, J.; Surendran, S.; Moon, B.; Sim, U. Efficient Photoelectrochemical Water Splitting Reaction using Electrodeposited Co_3Se_4 Catalyst. *Appl. Sci.* **2018**, *9*, 16. [CrossRef]
8. Stroyuk, O.; Raievska, O.; Zahn, D.R.T. Graphitic carbon nitride nanotubes: A new material for emerging applications. *RSC Adv.* **2020**, *10*, 34059–34087. [CrossRef]
9. de Oliveira, D.C.; Silva, W.O.; Chatenet, M.; Lima, F.H.B. NiOx-Pt/C nanocomposites: Highly active electrocatalysts for the electrochemical oxidation of hydrazine. *Appl. Catal. B Environ.* **2017**, *201*, 22–28. [CrossRef]
10. Ledendecker, M.; Calderón, S.K.; Papp, C.; Steinrück, H.-P.; Antonietti, M.; Shalom, M. The Synthesis of Nanostructured Ni_5P_4 Films and their Use as a Non-Noble Bifunctional Electrocatalyst for Full Water Splitting. *Angew. Chem. Int. Ed.* **2015**, *54*, 12361–12365. [CrossRef]
11. Han, H.S.; Park, W.; Hwang, S.W.; Kim, H.; Sim, Y.; Surendran, S.; Sim, U.; Cho, I.S. (0 2 0)-Textured tungsten trioxide nanostructure with enhanced photoelectrochemical activity. *J. Catal.* **2020**, *389*, 328–336. [CrossRef]
12. Chen, R.-R.; Ren, Q.-F.; Liu, Y.-X.; Ding, Y.; Zhu, H.-T.; Xiong, C.-Y.; Jin, Z.; Oh, W.-C. Synthesis of $\text{g-C}_3\text{N}_4$ /diatomite/ MnO_2 composites and their enhanced photo-catalytic activity driven by visible light. *J. Korean Ceram. Soc.* **2021**, *58*, 548–558. [CrossRef]
13. Huang, Y.; Ning, L.; Feng, Z.; Ma, G.; Yang, S.; Su, Y.; Hong, Y.; Wang, H.; Peng, L.; Li, J. Graphitic carbon nitride nanosheets with low ON1-doping content as efficient photocatalysts for organic pollutant degradation. *Environ. Sci. Nano* **2021**, *8*, 460–469. [CrossRef]

14. Cai, W.-Q.; Zhang, D.-F.; Zhang, F.-J.; Oh, W.-C. Preparation and photocatalytic activity of a novel BiOCl/g-C₃N₄ thin film prepared via spin coating. *J. Korean Ceram. Soc.* **2020**, *57*, 331–337. [[CrossRef](#)]
15. Huang, C.; Wen, Y.; Ma, J.; Dong, D.; Shen, Y.; Liu, S.; Ma, H.; Zhang, Y. Unraveling fundamental active units in carbon nitride for photocatalytic oxidation reactions. *Nat. Commun.* **2021**, *12*, 320. [[CrossRef](#)]
16. Wojtyła, S.; Śpiewak, K.; Baran, T. Synthesis, characterization and activity of doped graphitic carbon nitride materials towards photocatalytic oxidation of volatile organic pollutants emitted from 3D printer. *J. Photochem. Photobiol. A Chem.* **2020**, *391*, 112355. [[CrossRef](#)]
17. Wang, X.; Maeda, K.; Thomas, A.; Takahabe, K.; Xin, G.; Carlsson, J.M.; Domen, K.; Antonietti, M. A metal-free polymeric photocatalyst for hydrogen production from water under visible light. *Nat. Mater.* **2009**, *8*, 76–80. [[CrossRef](#)]
18. He, F.; Chen, G.; Zhou, Y.; Yu, Y.; Li, L.; Hao, S.; Liu, B. ZIF-8 derived carbon (C-ZIF) as a bifunctional electron acceptor and HER cocatalyst for g-C₃N₄: Construction of a metal-free, all carbon-based photocatalytic system for efficient hydrogen evolution. *J. Mater. Chem. A* **2016**, *4*, 3822–3827. [[CrossRef](#)]
19. Iqbal, N.; Khan, I.; Yamani, Z.H.; Qurashi, A. Sonochemical Assisted Solvothermal Synthesis of Gallium Oxynitride Nanosheets and their Solar-Driven Photoelectrochemical Water-Splitting Applications. *Sci. Rep.* **2016**, *6*, 32319. [[CrossRef](#)]
20. Sonya, K.; Yuriy, P.; Ivan, T.; Kazuma, M.; Jin, U.; Yutaka, K.; Kikuo, M.; Takeyoshi, S.; Takuya, M.; Daisuke, F.; et al. Tandem photovoltaic-photoelectrochemical GaAs/InGaAsP-WO₃/BiVO₄ device for solar hydrogen generation. *Jpn. J. Appl. Phys.* **2016**, *55*, 04ES01.
21. Bellardita, M.; García-López, E.I.; Marci, G.; Krivtsov, I.; García, J.R.; Palmisano, L. Selective photocatalytic oxidation of aromatic alcohols in water by using P-doped g-C₃N₄. *Appl. Catal. B Environ.* **2018**, *220*, 222–233. [[CrossRef](#)]
22. Jiménez-Salcedo, M.; Monge, M.; Tena, M.T. Photocatalytic degradation of ibuprofen in water using TiO₂/UV and g-C₃N₄/visible light: Study of intermediate degradation products by liquid chromatography coupled to high-resolution mass spectrometry. *Chemosphere* **2019**, *215*, 605–618. [[CrossRef](#)]
23. Navarro-Aguilar, A.I.; Obregón, S.; Sanchez-Martinez, D.; Hernández-Uresti, D.B. An efficient and stable WO₃/g-C₃N₄ photocatalyst for ciprofloxacin and orange G degradation. *J. Photochem. Photobiol. A Chem.* **2019**, *384*, 112010. [[CrossRef](#)]
24. Wang, J.; Xu, H.; Qian, X.; Dong, Y.; Gao, J.; Qian, G.; Yao, J. Direct Synthesis of Porous Nanorod-Type Graphitic Carbon Nitride/CuO Composite from Cu-Melamine Supramolecular Framework towards Enhanced Photocatalytic Performance. *Chem. Asian J.* **2015**, *10*, 1276–1280. [[CrossRef](#)]
25. Rahman, M.; Davey, K.; Mullins, C.B. Tuning the Intrinsic Properties of Carbon Nitride for High Quantum Yield Photocatalytic Hydrogen Production. *Adv. Sci.* **2018**, *5*, 1800820. [[CrossRef](#)]
26. Liu, X.; Iocozzia, J.; Wang, Y.; Cui, X.; Chen, Y.; Zhao, S.; Li, Z.; Lin, Z. Noble metal-metal oxide nanohybrids with tailored nanostructures for efficient solar energy conversion, photocatalysis and environmental remediation. *Energy Environ. Sci.* **2017**, *10*, 402–434. [[CrossRef](#)]
27. Niu, P.; Yang, Y.; Yu, J.C.; Liu, G.; Cheng, H.-M. Switching the selectivity of the photoreduction reaction of carbon dioxide by controlling the band structure of a g-C₃N₄ photocatalyst. *Chem. Commun.* **2014**, *50*, 10837–10840. [[CrossRef](#)]
28. Yuan, L.; Xu, Y.-J. Photocatalytic conversion of CO₂ into value-added and renewable fuels. *Appl. Surf. Sci.* **2015**, *342*, 154–167. [[CrossRef](#)]
29. Liu, H.; Wu, P.; Li, H.; Chen, Z.; Wang, L.; Zeng, X.; Zhu, Y.; Jiang, Y.; Liao, X.; Haynes, B.S.; et al. Unravelling the effects of layered supports on Ru nanoparticles for enhancing N₂ reduction in photocatalytic ammonia synthesis. *Appl. Catal. B Environ.* **2019**, *259*, 118026. [[CrossRef](#)]
30. Zhang, M.; Wang, X. Two dimensional conjugated polymers with enhanced optical absorption and charge separation for photocatalytic hydrogen evolution. *Energy Environ. Sci.* **2014**, *7*, 1902–1906. [[CrossRef](#)]
31. Wang, Y.; Xu, Y.; Wang, Y.; Qin, H.; Li, X.; Zuo, Y.; Kang, S.; Cui, L. Synthesis of Mo-doped graphitic carbon nitride catalysts and their photocatalytic activity in the reduction of CO₂ with H₂O. *Catal. Commun.* **2016**, *74*, 75–79. [[CrossRef](#)]
32. Su, F.; Mathew, S.C.; Lipner, G.; Fu, X.; Antonietti, M.; Blechert, S.; Wang, X. mpg-C₃N₄-Catalyzed Selective Oxidation of Alcohols Using O₂ and Visible Light. *J. Am. Chem. Soc.* **2010**, *132*, 16299–16301. [[CrossRef](#)] [[PubMed](#)]
33. Butchosa, C.; Guiglian, P.; Zwiijnenburg, M.A. Carbon Nitride Photocatalysts for Water Splitting: A Computational Perspective. *J. Phys. Chem. C* **2014**, *118*, 24833–24842. [[CrossRef](#)]
34. Martin, D.J.; Qiu, K.; Shevlin, S.A.; Handoko, A.D.; Chen, X.; Guo, Z.; Tang, J. Highly Efficient Photocatalytic H₂ Evolution from Water using Visible Light and Structure-Controlled Graphitic Carbon Nitride. *Angew. Chem. Int. Ed.* **2014**, *53*, 9240–9245. [[CrossRef](#)]
35. Habisreutinger, S.; Schmidt-Mende, L.; Stolarczyk, J.K. Photocatalytic Reduction of CO₂ on TiO₂ and Other Semiconductors. *Angew. Chem. Int. Ed.* **2013**, *52*, 7372–7408. [[CrossRef](#)] [[PubMed](#)]
36. Jorge, A.B.; Martin, D.J.; Dhanoa, M.T.S.; Rahman, A.S.; Makwana, N.; Tang, J.; Sella, A.; Corà, F.; Firth, S.; Darr, J.A.; et al. H₂ and O₂ Evolution from Water Half-Splitting Reactions by Graphitic Carbon Nitride Materials. *J. Phys. Chem. C* **2013**, *117*, 7178–7185. [[CrossRef](#)]
37. Guan, M.; Wang, Q.; Zhang, X.; Bao, J.; Gong, X.; Liu, Y. Two-Dimensional Transition Metal Oxide and Hydroxide-Based Hierarchical Architectures for Advanced Supercapacitor Materials. *Front. Chem.* **2020**, *8*, 390. [[CrossRef](#)]
38. Fang, S.; Bresser, D.; Passerini, S. Transition Metal Oxide Anodes for Electrochemical Energy Storage in Lithium- and Sodium-Ion Batteries. *Adv. Energy Mater.* **2019**, *10*, 1902485. [[CrossRef](#)]

39. Xu, J.; Yu, H.; Guo, H. Synthesis and behaviors of g-C₃N₄ coupled with La_xCo_{3-x}O₄ nanocomposite for improved photocatalytic activity and stability under visible light. *Mater. Res. Bull.* **2018**, *105*, 342–348. [[CrossRef](#)]
40. Modak, B.; Ghosh, S.K. Exploring the Role of La Codoping beyond Charge Compensation for Enhanced Hydrogen Evolution by Rh–SrTiO₃. *J. Phys. Chem. B* **2015**, *119*, 11089–11098. [[CrossRef](#)]
41. Jin, L.; Zhou, X.; Ning, X.; Zhan, L.; Kong, M.; Tan, K.; Li, J.; Lin, Z. Boosting visible light photocatalytic performance of g-C₃N₄ nanosheets by combining with LaFeO₃ nanoparticles. *Mater. Res. Bull.* **2018**, *102*, 353–361. [[CrossRef](#)]
42. Li, N.; Jayaraman, S.; Tee, S.Y.; Kumar, P.S.; Lee, C.J.J.; Liew, S.L.; Chi, D.; Hor, T.S.A.; Ramakrishna, S.; Luo, H.-K. Effect of La-Doping on optical bandgap and photoelectrochemical performance of hematite nanostructures. *J. Mater. Chem. A* **2014**, *2*, 19290–19297. [[CrossRef](#)]
43. Arabi, A.; Fazli, M.; Ehsani, M. Tuning the morphology and photocatalytic activity of La_{0.7}Ca_{0.3}MnO₃ nanorods via different mineralizer-assisted hydrothermal syntheses. *Mater. Res. Bull.* **2017**, *90*, 205–211. [[CrossRef](#)]
44. Zeng, Z.; Li, K.; Yan, L.; Dai, Y.; Guo, H.; Huo, M.; Guo, Y. Fabrication of carbon nitride nanotubes by a simple water-induced morphological transformation process and their efficient visible-light photocatalytic activity. *RSC Adv.* **2014**, *4*, 59513–59518. [[CrossRef](#)]
45. Rehman, A.; Ehsan, M.A.; Afzal, A.; Ali, A.; Iqbal, N. Aerosol-assisted nanostructuring of nickel/cobalt oxide thin films for viable electrochemical hydrazine sensing. *Analyst* **2021**, *146*, 3317–3327. [[CrossRef](#)] [[PubMed](#)]
46. Ehsan, M.A.; Aziz, A.; Rehman, A.; Hakeem, A.S.; Qasem, M.A.A.; Saadi, O.W. Facile Synthesis of Gold-Supported Thin Film of Cobalt Oxide via AACVD for Enhanced Electrocatalytic Activity in Oxygen Evolution Reaction. *ECS J. Solid State Sci. Technol.* **2018**, *7*, P711–P718. [[CrossRef](#)]
47. Pathan, A.A.; Desai, K.R.; Bhasin, C. Synthesis of La₂O₃ Nanoparticles using Glutaric acid and Propylene glycol for Future CMOS Applications. *Int. J. Nanomater. Chem.* **2017**, *3*, 21–25. [[CrossRef](#)]
48. Iqbal, N.; Afzal, A.; Khan, I.; Khan, M.S.; Qurashi, A. Molybdenum impregnated g-C₃N₄ nanotubes as potentially active photocatalyst for renewable energy applications. *Sci. Rep.* **2021**, *11*, 16886. [[CrossRef](#)]
49. Iqbal, N.; Khan, I.; Ali, A.; Qurashi, A. A sustainable molybdenum oxysulphide-cobalt phosphate photocatalyst for effectual solar-driven water splitting. *J. Adv. Res.* **2021**. [[CrossRef](#)]
50. Han, C.; Ge, L.; Chen, C.; Li, Y.; Xiao, X.; Zhang, Y.; Guo, L. Novel visible light induced Co₃O₄-g-C₃N₄ heterojunction photocatalysts for efficient degradation of methyl orange. *Appl. Catal. B Environ.* **2014**, *147*, 546–553. [[CrossRef](#)]
51. Hou, Y.; Li, J.; Wen, Z.; Cui, S.; Yuan, C.; Chen, J. Co₃O₄ nanoparticles embedded in nitrogen-doped porous carbon dodecahedrons with enhanced electrochemical properties for lithium storage and water splitting. *Nano Energy* **2015**, *12*, 1–8. [[CrossRef](#)]
52. Wei, W.-D.; Liu, X.-Y.; Cui, S.-C.; Liu, J.-G. Loading of Co₃O₄ onto Pt-modified nitrogen-doped TiO₂ nanocomposites promotes photocatalytic hydrogen production. *RSC Adv.* **2017**, *7*, 25650–25656. [[CrossRef](#)]
53. Goodall, J.B.M.; Kellici, S.; Illsley, D.; Lines, R.; Knowles, J.C.; Darr, J.A. Optical and photocatalytic behaviours of nanoparticles in the Ti–Zn–O binary system. *RSC Adv.* **2014**, *4*, 31799–31809. [[CrossRef](#)]
54. Schevciw, O.; White, W.B. The optical absorption edge of rare earth sesquisulfides and alkaline earth-rare earth sulfides. *Mater. Res. Bull.* **1983**, *18*, 1059–1068. [[CrossRef](#)]
55. Köferstein, R.; Jäger, L.; Ebbinghaus, S. Magnetic and optical investigations on LaFeO₃ powders with different particle sizes and corresponding ceramics. *Solid State Ionics* **2013**, *249–250*, 1–5. [[CrossRef](#)]
56. Huang, X.; Hao, H.; Liu, Y.; Zhu, Y.; Zhang, X. Rapid Screening of Graphitic Carbon Nitrides for Photocatalytic Cofactor Regeneration Using a Drop Reactor. *Micromachines* **2017**, *8*, 175. [[CrossRef](#)]
57. Ferrari, A.C.; Rodil, S.E.; Robertson, J. Interpretation of infrared and Raman spectra of amorphous carbon nitrides. *Phys. Rev. B* **2003**, *67*, 155306. [[CrossRef](#)]
58. Jürgens, B.; Irran, E.; Senker, J.; Kroll, P.; Müller, H.; Schnick, W. Melem (2,5,8-Triamino-tri-s-triazine), an Important Intermediate during Condensation of Melamine Rings to Graphitic Carbon Nitride: Synthesis, Structure Determination by X-ray Powder Diffractometry, Solid-State NMR, and Theoretical Studies. *J. Am. Chem. Soc.* **2003**, *125*, 10288–10300. [[CrossRef](#)] [[PubMed](#)]
59. Saleem, M.; Sharma, M.; Mahajan, S.; Sheikh, H.N.; Kalsotra, B.L. Synthesis and Characterization of Group-6 Metal Carbonyl Complexes of Aroyl Hydrazone Derivatives. *E-J. Chem.* **2012**, *9*, 807–817. [[CrossRef](#)]
60. Zhang, S.; Li, J.; Zeng, M.; Li, J.; Xu, J.; Wang, X. Bandgap Engineering and Mechanism Study of Nonmetal and Metal Ion Codoped Carbon Nitride: C+Fe as an Example. *Chem. Eur. J.* **2014**, *20*, 9805–9812. [[CrossRef](#)]
61. Wang, H.; Yang, Y.; Li, Q.; Lu, W.; Ning, J.; Zhong, Y.; Zhang, Z.; Hu, Y. Molecule-assisted modulation of the high-valence Co³⁺ in 3D honeycomb-like CoxSy networks for high-performance solid-state asymmetric supercapacitors. *Sci. China Mater.* **2021**, *64*, 840–851. [[CrossRef](#)]
62. Niu, H.; Liu, Y.; Mao, B.; Xin, N.; Jia, H.; Shi, W. In-situ embedding MOFs-derived copper sulfide polyhedrons in carbon nanotube networks for hybrid supercapacitor with superior energy density. *Electrochim. Acta* **2020**, *329*, 135130. [[CrossRef](#)]
63. Li, L.; Guo, C.; Shen, J.; Ning, J.; Zhong, Y.; Hu, Y. Construction of sugar-gourd-shaped CdS/Co_{1-x}S hollow hetero-nanostructure as an efficient Z-scheme photocatalyst for hydrogen generation. *Chem. Eng. J.* **2020**, *400*, 125925. [[CrossRef](#)]
64. Alkaykh, S.; Mbarek, A.; Ali-Shattle, E.E. Photocatalytic degradation of methylene blue dye in aqueous solution by MnTiO₃ nanoparticles under sunlight irradiation. *Heliyon* **2020**, *6*, e03663. [[CrossRef](#)] [[PubMed](#)]
65. Matthews, R.W. Purification of water with near—u.v. illuminated suspensions of titanium dioxide. *Water Res.* **1990**, *24*, 653–660. [[CrossRef](#)]

66. He, H.Y.; Dong, W.X.; Zhang, G.H. Photodegradation of aqueous methyl orange on MnTiO₃ powder at different initial pH. *Res. Chem. Intermed.* **2010**, *36*, 995–1001. [[CrossRef](#)]
67. Azeez, F.; Al-Hetlani, E.; Arafa, M.; Abdelmonem, Y.; Nazeer, A.A.; Amin, M.O.; Madkour, M. The effect of surface charge on photocatalytic degradation of methylene blue dye using chargeable titania nanoparticles. *Sci. Rep.* **2018**, *8*, 7104. [[CrossRef](#)] [[PubMed](#)]
68. Kuila, S.K.; Sarkar, R.; Kumbhakar, P.; Kumbhakar, P.; Tiwary, C.S.; Kundu, T.K. Photocatalytic dye degradation under sunlight irradiation using cerium ion adsorbed two-dimensional graphitic carbon nitride. *J. Environ. Chem. Eng.* **2020**, *8*, 103942. [[CrossRef](#)]